Drop impact onto a liquid layer of finite thickness: Dynamics of the cavity evolution

Edin Berberović,* Nils P. van Hinsberg, Suad Jakirlić, Ilia V. Roisman, and Cameron Tropea
Technische Universität Darmstadt, Chair of Fluid Mechanics and Aerodynamics, Petersenstraße 30, 64287 Darmstadt, Germany
(Received 24 November 2008; published 18 March 2009)

In the present work experimental, numerical, and theoretical investigations of a normal drop impact onto a liquid film of finite thickness are presented. The dynamics of drop impact on liquid surfaces, the shape of the cavity, the formation and propagation of a capillary wave in the crater, and the residual film thickness on the rigid wall are determined and analyzed. The shape of the crater within the film and the uprising liquid sheet formed upon the impact are observed using a high-speed video system. The effects of various influencing parameters such as drop impact velocity, liquid film thickness and physical properties of the liquids, including viscosity and surface tension, on the time evolution of the crater formation are investigated. Complementary to experiments the direct numerical simulations of the phenomena are performed using an advanced free-surface capturing model based on a two-fluid formulation of the classical volume-of-fluid (VOF) model in the framework of the finite volume numerical method. In this model an additional convective term is introduced into the transport equation for phase fraction, contributing decisively to a sharper interface resolution. Furthermore, an analytical model for the penetration depth of the crater is developed accounting for the liquid inertia, viscosity, gravity, and surface tension. The model agrees well with the experiments at the early times of penetration far from the wall if the impact velocity is high. Finally, a scaling analysis of the residual film thickness on the wall is conducted demonstrating a good agreement with the numerical predictions.

DOI: 10.1103/PhysRevE.79.036306 PACS number(s): 47.55.dr, 47.55.nd, 47.11.Df

I. INTRODUCTION

Splashing of drops on liquid layers is encountered frequently in nature and leads to various phenomena such as air bubble formation during heavy rain, formation of a crownlike liquid sheet with detaching secondary droplets, and ejection of a liquid jet from the region of impact. Investigations of drop impact onto liquid films have also importance in various ecological and engineering fields: soil erosion, dispersion of seed and microorganisms, spray coating and cooling, paint spraying and internal combustion engines with direct fuel injection, where the fuel is sprayed into engine cylinders in the form of small droplets which splash on the inner walls oil films of cylinders.

The phenomena involved in drop impact onto various surfaces were the subject of experimental, numerical, and also theoretical studies, a comprehensive review can be found in [1]. The sequence of events which occurs during the impact of single drops onto films or pools of various depths has been described in [2]. Much research has been conducted to understand the evolution of the maximum crater depth in relation to the crown formation, splashing, the Worthington jet height, and bubble entrainment during single drop impact onto thin and deep liquid pools. Less attention, however, has been paid to the phenomena taking place below the surface, in particular the evolution of the impact crater in shallow pools [3–5], which is important for spray cooling.

An interesting phenomenon, which appears at almost every drop impact onto a shallow or deep pool, is the formation of a capillary wave after impact. This concentric capillary ripple travels along the crater sidewall and changes the shape of the crater from hemispherical for deep pools or from oblate for shallow pools to a conical shape. In [6–8] the origin of this traveling capillary wave was related to the strong surface disturbance immediately after the initial contact of the impacting drop with the undisturbed liquid surface. For deep pools, several authors found that when this capillary wave reaches the bottom of the crater at a certain time instant, its crest closes concentrically to trap an air bubble [7,9,10]. The inertia dominated capillary waves on a nearly planar liquid, radially expanding lamella resulting from drop impact are well understood. The analysis of such waves can be found in [11]. Some other capillary waves resulting from drop impact on films were reported in [12], which even lead to the ejection of jet.

Rapid advances in computer hardware and developments of numerical algorithms have enabled a broader use of computational methods for investigating the drop impact phenomena. Numerical simulations provide a detailed database comprising not only the dynamics of the drop surface with respect to its position and form but also the temporal behavior of entire velocity and pressure fields, the latter being beyond the reach of the existing experimental methods. Because of their importance, numerous computational studies of these flows have been reported in the literature. We mention here only some relevant publications [13–15]

The main subject of the present study is the experimental, numerical, and theoretical investigations of a normal drop impact onto a liquid film of a finite thickness. The formation and evolution of the crater formed within the film upon the impact are investigated for various film thicknesses, drop impact velocities, and using three different liquids. The study focuses on the description of the crater penetration, expansion, formation of the residual film on the substrate, as well as on the emergence and propagation of a sharp-edged axisymmetric capillary wave leading to the crater retraction.

*Also at Chair of Energy Technology and Process Engineering, University of Zenica, Fakultetska 1, 72000 Zenica, Bosnia and Herzegovina.

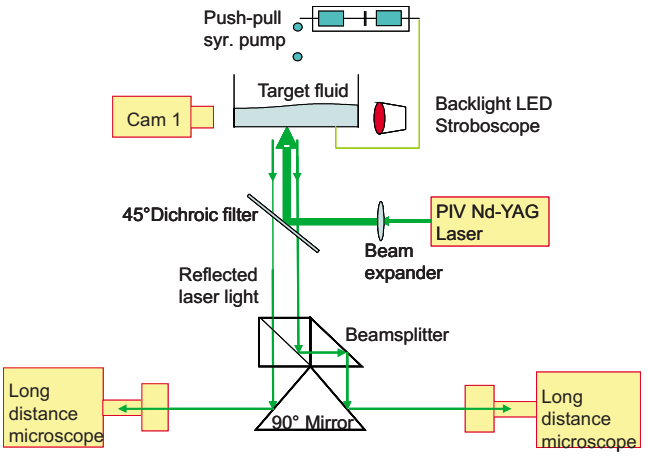

FIG. 1. (Color online) Experimental setup.

II. EXPERIMENTAL INVESTIGATIONS

Experimental measurements were performed using the experimental setup shown in Fig. 1. Drops are generated using a syringe pump with a constant preset flow rate. The drop is formed at the tip of the needle and grows until its weight exceeds the surface tension force.

After the drop detaches from the needle it falls and passes a light barrier before reaching the center of a cylindrical dish of 90 mm diameter made of plexiglas. The cylinder is large enough to avoid effects of wave reflections from the sides with the impact process. The light barrier activates an electronic delay circuit that triggers the imaging system, consisting of two charge-coupled device (CCD) cameras, one backlit by a stroboscope and the other by a particle image velocimetry (PIV) laser.

In order to investigate the influence of liquid properties on the crater evolution, three liquids were used: distilled water, isopropanol, and a glycerin-water mixture consisting of 70% glycerin and 30% water. The fluid of the drop and the film is the same in all experiments.

Comparison of different cases is enabled by the use of the nondimensional numbers governing the impact process: Weber number $\mathrm{We}=\rho U^2 D/\sigma$ giving the relation of inertial to surface tension forces, Ohnesorge number $\mathrm{Oh}=\mu/(\sigma\rho D)^{1/2}$ giving the relation of viscous to surface tension forces, Reynolds number $\mathrm{Re}=UD/\nu$ giving the relation of inertial to viscous forces, Froude number $\mathrm{Fr}=U^2/(gD)$ giving the relation of inertial forces to gravity, dimensionless film thickness $\bar{H}=H/D$, and dimensionless time $\bar{t}=tU/D$. In the above expressions μ, σ, and ρ are dynamic viscosity, surface tension coefficient, and density of the liquids used, D and U are the diameter and the impact velocity of the drop, and H is the initial film thickness. One of the parameters characterizing splashing threshold is the well-known $K=\mathrm{We}/\mathrm{Oh}^{0.4}$ parameter [16]. This parameter can be represented as a combination of the Weber and Reynolds numbers. Nevertheless, this parameter is added in the description of the results in order to characterize the impact parameters with respect to the splashing threshold. The initial drop diameter is 2.9 mm for distilled water, 2.14 mm for isopropanol, and 2.67 mm for glycerin-water mixture. The drop impact velocity (velocity just before the drop reaches the film surface) is calculated from a distance measurement and a preset time delay between subsequent exposures. Thus, for distilled water the impact velocity varied from 1.68 m/s to 2.91 m/s, for isopropanol from 1.7 m/s to 2.83 m/s and for glycerin-water mixture from 1.81 m/s to 3.25 m/s. The liquid film thickness was varied for all liquids, yielding the nondimensional film thickness of 0.5 to 2. The film thickness is held constant by means of the push-pull syringe pump, which sucks the same amount of liquid from the film as is added by the impacting drops, with an error in thickness of 3% to 7% for distilled water, 2% to 10% for isopropanol, and 1% to 5% for the glycerin-water mixture.

The physical properties of liquids and ranges of the nondimensional numbers are given in Table I.

III. THEORETICAL MODEL FOR THE PENETRATION DEPTH AT THE INITIAL STAGE

In most of the existing theoretical studies of drop impact into a deep pool the cavity penetration is described using the energy balance approach [4,17–19], where the shape of the crater is approximated by an expanding sphere. Such approximation is based on the assumption that the cavity expands equally in all directions.

In this section we develop a theoretical model for the cavity penetration in a semi-infinity liquid based only on the linear momentum balance of the liquid around the cavity.

Consider the penetration of the cavity shown schematically in Fig. 2, and a spherical coordinate system $\{r,\theta,\phi\}$ with the origin fixed at the point of impact at the initial film

TABLE I. Physical properties of the liquids used (at 20 °C) and the ranges of nondimensional numbers.

	Distilled water	Isopropanol	Glycerin water mixture
Density, ρ (kg/m^3)	999	805	1179
Viscosity, μ (Ns/m^2)	9.9×10^{-4}	2.3×10^{-3}	18.57×10^{-3}
Surface tension, σ (N/m)	7.27×10^{-2}	2.36×10^{-2}	6.68×10^{-2}
Ohnesorge number	0.0021	0.0112	0.0409
Weber number	113–312	189–644	151–505
Reynolds number	4744–8587	1200–2010	299–561
K parameter	1331–3675	1101–3883	524–1814

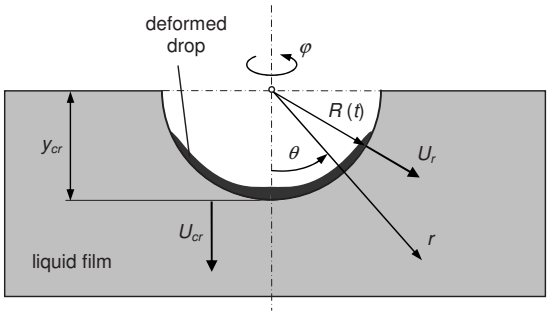

FIG. 2. Sketch of the penetrating cavity.

level. The penetration depth of the crater is denoted y_{cr} and the penetration speed is denoted $U_{cr}=\dot{y}_{cr}$.

Since the impacting drop deforms during penetration, the penetration depth can be roughly approximated by the position of the drop and/or film interface at the impact axis. The penetration depth initially increases with almost constant velocity, which is approximately half of the impact velocity and depends only weakly on the surface tension, viscosity, or film thickness. The velocity of high-speed jet penetration whose density equals the density of the target, $U_{cr}\approx 1/2U$ is well known in penetration mechanics (see, for example, the study on the penetration jets generated by shaped charges [20] or eroding metal projectile into an elastic-plastic target [21]). The corresponding penetration depth is $y_{cr}\approx Ut/2$. The duration of this stage is finite, $t=2D/U$. It is determined by the rate of the drop erosion, which is proportional to $U-U_{cr}$.

At the times $t>2D/U$ the cavity propagates only due to the inertia of the flow in the liquid film and decelerates. In order to estimate the flow in the film at this stage we approximate the shape of the crater as a spherical cavity with the center coinciding with the origin of the coordinate system fixed at the point of impact. This flow is similar to the flow induced by a single spherical bubble changing in size, produced by an underwater explosion [22]. If the penetration depth is much smaller than the initial film thickness, the flow around the cavity can be approximated by a potential velocity field in the semi-infinite space. The velocity field in liquid in that case is given by [22]

$$v_r=\frac{R^2}{r^2}\dot{R},\quad v_\theta=v_\varphi=0, \tag{1}$$

and the corresponding velocity potential by

$$\phi=-\frac{R^2}{r}\dot{R} \tag{2}$$

where $R=R(t)$ is the expanding radius of the cavity and $\dot{R}=dR/dt$ is the radial velocity of propagation of cavity surface.

If the Froude number is much higher than unity the effect of gravity at the initial stage of cavity expansion is negligibly small. If the penetration depth is much smaller than the capillary length, the deviation of the cavity shape from the sphere can also be neglected. The expression for the pressure field $p(r,t)$ in the liquid can be obtained from the Bernoulli equation in the following form:

$$\frac{\partial\phi}{\partial t}+\frac{1}{2}v_r^2+\frac{p}{\rho}=f(t), \tag{3}$$

where $f(t)$ is a function of time only. It can be shown that $f(t)=0$ since the liquid velocity vanishes at $r\to\infty$. Substituting the expressions for the liquid velocity (1) and potential (2) in the equation (3) yields the following expression for the pressure distribution at the cavity surface ($r=R$):

$$p_{cr}=\rho\ddot{R}R+\rho\frac{3\dot{R}^2}{2}. \tag{4}$$

It should be noted that this pressure field is valid even if the viscosity of the liquid is significant. The viscous part of the radial component of the stress tensor at the cavity surface is of order $4\mu\dot{R}/R$, the pressure jump associated with the surface tension is $2\sigma/R$, and the hydrostatic pressure is ρgR. These terms are negligibly small in comparison with the inertial stresses expressed in Eq. (4) if the Reynolds, Weber, and Froude numbers are much higher than the unity. In this case the equation of the cavity penetration and expansion can be obtained form the condition that the pressure in the liquid vanishes at the cavity surface.

Moreover, in our model the penetration depth y_{cr} of the crater is equal to the cavity radius R (see Fig. 2). The asymptotic equation for the crater penetration can be written with the help of Eq. (4) in the following dimensionless form:

$$\bar{y}_{cr}=-\frac{3\ddot{\bar{y}}_{cr}^2}{2\dot{\bar{y}}_{cr}}. \tag{5}$$

Equation (5) has the form similar to the equation of rising of a spherical-cap bubble [22].

We should emphasize that this equation for the crater penetration is valid only for the initial stage of crater penetration when the deformation of the shape of the spherical cavity due to the gravity and capillary effects is negligibly small.

The corresponding analytical solution for the crater depth is

$$\bar{y}_{cr}=2^{-4/5}(5\bar{t}-6)^{2/5},\quad \bar{t}>2. \tag{6}$$

In Fig. 3 the experimental data from [17,23] for the penetration depth of the crater is compared with the theoretical predictions. In the case of high impact Weber and Froude numbers the asymptotic formula (6) agrees very well with the experiments. In the case of relatively smaller impact velocity the influence of the gravity, viscosity and surface tension become significant leading to some deviation form the asymptotic solution and even to the damping of the penetration by gravity and capillary forces which are not accounted for in the approximate solution (6).

It should be noted that the receding of the cavity diameter can differ significantly from the receding of the cavity in the axial direction, leading to a decrease of the cavity penetration length. In this stage the shape of the cavity changes significantly due to occurrence of capillary waves. Moreover,

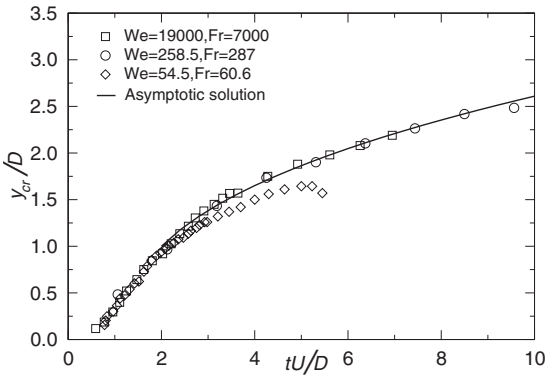

FIG. 3. Drop impact onto a deep pool: comparison of the asymptotic solution (6) for the penetration depth of the cavity with the experimental data from [17,23].

in some cases when the cavity diameter recedes while the tip continues to penetrate, the impact leads to the formation of bubble entrainment [23]. The cavity form at this stage cannot be approximated by the simple shape of a sphere. Therefore, the theory is not valid for the receding phase of the cavity expansion. The asymptotic solution (6) for the penetration depth agrees well with the experimental data at the initial stage of penetration if the Reynolds and Weber numbers are high.

The experimental data for the crater penetration length for various impact parameters and initial film thicknesses is shown in Fig. 4 in comparison with the theoretical predictions. The deviation from Eq. (6) is determined by the initial film thickness, or more precisely, by the vicinity of the crater tip to the rigid substrate. For example, the case with We $=315$ corresponds to $\bar{H}=2$ whereas the case with We$=328$ corresponds to $\bar{H}=1$ leading to earlier deviation from the theory developed for deep pool. These results also demonstrate that wall effects may be significant already at the initial stages of drop impact. The most reliable way to predict such phenomena is using the direct numerical simulations of the flow.

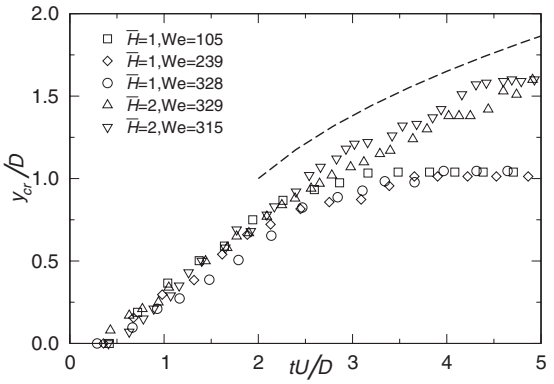

FIG. 4. Drop impact onto a liquid film of finite thickness: experimentally obtained penetration depth of the cavity (symbols) as a function of time for various film thicknesses compared to the asymptotic solution (6)

IV. NUMERICAL PREDICTIONS

A. Mathematical model

Complementary to the experiments, numerical simulations of the cases studied were performed. The process of drop impact is generally difficult to simulate because of its highly transient nature. The length scales the thin free sheets and thin wall films produced by drop impact are often several orders smaller than the initial drop diameter. Therefore, a reliable simulation of the drop impact phenomena requires an extremely fine numerical mesh.

The physics of this phenomenon dictates that there are several competitive effects influencing the flow field during impact and the final outcome after the impact: gravity, viscous, inertial, and surface tension forces. For example, when the crater has reached maximum diameter and depth, inertia becomes less significant and surface tension governs the receding motion of the crater. Capillary effects are responsible for the formation of the rim at the edge of a free liquid sheet [24] or propagation of capillary waves.

In the conventional volume-of-fluid (VOF) method [25], the transport equation for an indicator function, representing the volume fraction of one phase, is solved simultaneously with the continuity and momentum equations,

$$\nabla \cdot \mathbf{U} = 0, \tag{7}$$

$$\frac{\partial \gamma}{\partial t} + \nabla \cdot (\mathbf{U}\gamma) = 0, \tag{8}$$

$$\frac{\partial(\rho \mathbf{U})}{\partial t} + \nabla \cdot (\rho \mathbf{U}\mathbf{U}) = -\nabla p + \nabla \cdot \mathbf{T} + \rho \mathbf{f}_b, \tag{9}$$

where $\mathbf{U}$ represents the velocity field shared by the two fluids throughout the flow domain, γ is the phase fraction, $\mathbf{T}$ is the deviatoric viscous stress tensor $\{\mathbf{T}=2\mu\mathbf{S}-2\mu(\nabla\cdot\mathbf{U})\mathbf{I}/3$, with the mean rate of strain tensor $\mathbf{S}=0.5[\nabla\mathbf{U}+(\nabla\mathbf{U})^T]$ and $\mathbf{I} \equiv \delta_{ij}\}$, ρ is density, p is pressure, and $\mathbf{f}_b$ are body forces per unit mass. In VOF simulations the latter forces include gravity and surface tension effects at the interface. The phase fraction γ can take values within the range $0 \leqslant \gamma \leqslant 1$, with the values of zero and one corresponding to regions accommodating only one phase, e.g., $\gamma=0$ for gas and $\gamma=1$ for liquid. Accordingly, gradients of the phase fraction are encountered only in the region of the interface.

Two immiscible fluids are considered as one effective fluid throughout the domain, the physical properties of which are calculated as weighted averages based on the distribution of the liquid volume fraction, thus being equal to the properties of each fluid in their corresponding occupied regions and varying only across the interface,

$$\rho = \rho_l \gamma + \rho_g (1-\gamma), \tag{10}$$

$$\mu = \mu_l \gamma + \mu_g (1-\gamma), \tag{11}$$

where ρ_l and ρ_g are densities of liquid and gas, respectively.

One of the critical issues in numerical simulations of free surface flows using the VOF model is the conservation of the phase fraction. This is especially the case in flows with high

density ratios, where small errors in volume fraction may lead to significant errors in calculations of physical properties. Accurate calculation of the phase fraction distribution is crucial for a proper evaluation of surface curvature, which is required for the determination of surface tension force and the corresponding pressure gradient across the free surface. The interface region between two phases is typically smeared over a few grid cells and is therefore highly sensitive to grid resolution.

It is not a simple task to assure boundedness and conservativeness of the phase fraction. Various attempts have been made in order to overcome these difficulties [26–29]. Furthermore, the definition of velocity by which the free surface is advanced, as a single velocity being shared by both phases, is misleading, e.g., no conclusion can be made as to what extent the velocity of each particular phase contributes to the velocity of the effective fluid.

In the present study a modified approach similar to one proposed in [30] is used, with an advanced model formulated by OpenCFD Ltd. [31], relying on a two-fluid formulation of the conventional volume-of-fluid model in the framework of the finite volume method. Its systematic derivation is outlined below. In this model an additional convective term originating from modeling the velocity in terms of a weighted average of the corresponding liquid and gas velocities is introduced into the transport equation for phase fraction, providing a sharper interface resolution. The model makes use of the two-fluid Eulerian model for two-phase flow, where phase fraction equations are solved separately for each individual phase [32]; hence the equations for each of the phase fractions can be expressed as

$$\frac{\partial \gamma}{\partial t} + \nabla \cdot (\mathbf{U}_l \gamma) = 0, \tag{12}$$

$$\frac{\partial (1-\gamma)}{\partial t} + \nabla \cdot [\mathbf{U}_g (1-\gamma)] = 0, \tag{13}$$

where the subscripts l and g denote the liquid and gaseous phase, respectively. Assuming that the contributions of the liquid and gas velocities to the evolution of the free surface are proportional to the corresponding phase fraction, and defining the velocity of the effective fluid in a VOF model as a weighted average [33],

$$\mathbf{U} = \gamma \mathbf{U}_l + (1-\gamma)\mathbf{U}_g, \tag{14}$$

Eq. (12) can be rearranged and used as an evolution equation for the phase fraction γ,

$$\frac{\partial \gamma}{\partial t} + \nabla \cdot (\mathbf{U}\gamma) + \nabla \cdot [\mathbf{U}_r \gamma (1-\gamma)] = 0, \tag{15}$$

where $\mathbf{U}_r = \mathbf{U}_l - \mathbf{U}_g$ is the vector of relative velocity, designated as the "compression velocity."

Accordingly, the equation governing the volume fraction [Eq. (15)] contains an additional convective term, referred to as the "compression term" keeping in mind its role to "compress" the free surface towards a sharper one (it should be noted that the wording compression represents just a denotation and does not relate to compressible flow). In comparison to Eq. (8), this term appears as an artificial contribution to convection of the phase fraction, but since the derivation of Eq. (15) relies on the velocity defined by Eq. (14), a strong coupling between the classical VOF and a two-fluid model is achieved. The additional convective term contributes significantly to a higher interface resolution, thus avoiding the need to devise a special scheme for convection, such as CICSAM [34]. This term is active only within the interface region and vanishes at both limits of the phase fraction. Therefore it does not affect the solution outside this region. Moreover if the free surface is defined in a theoretical sense as having an infinitesimally small thickness, the (relative) velocity $\mathbf{U}_r$ vanishes and the expression (15) reduces to the conventional form (8).

In addition to properly reflecting the physics of the flow, the main advantage of such formulation is in the possibility of capturing the interface region much more sharply in comparison to the classical VOF approach. Numerical diffusion, unavoidably introduced through the discretization of convective terms, can be controlled and minimized through the discretization of the compression term, thus allowing sharp interface resolution. The details of its numerical treatment are given in Sec. IV B 2. To our knowledge, this is the first application of such a free-surface resolving model to the drop impact onto a liquid film.

The momentum equation, Eq. (9), is modified in order to account for the effects of surface tension. The surface tension at the liquid-gas interface generates an additional pressure gradient resulting in a force, which is evaluated per unit volume using the continuum surface force (CSF) model [35],

$$\mathbf{f}_\sigma = \sigma \kappa \nabla \gamma. \tag{16}$$

where κ is the mean curvature of the free surface, determined from the expression

$$\kappa = -\nabla \cdot \left(\frac{\nabla \gamma}{|\nabla \gamma|} \right). \tag{17}$$

Equation (16) is only valid for the cases with constant surface tension, as considered here. In the case of variable surface tension, e.g., due to nonuniformly distributed temperature, surface tension gradients are encountered, generating an additional shear stress at the interface, which should be taken into account.

Both fluids are considered to be Newtonian and incompressible ($\nabla \cdot \mathbf{U} = 0$), and the rate of strain tensor is linearly related to the stress tensor, which is decomposed into a more convenient form for discretization,

$$\nabla \cdot \mathbf{T} = \mu [\nabla \mathbf{U} + (\nabla \mathbf{U})^T] = \nabla \cdot (\mu \nabla \mathbf{U}) + (\nabla \mathbf{U}) \cdot \nabla \mu. \tag{18}$$

In a single pressure system as considered for the present VOF method, the normal component of the pressure gradient at a stationary nonvertical solid wall, with no-slip condition on velocity, must be different for each phase due to the hydrostatic component ρg when the phases are separated at the wall, i.e., if a contact line exists. In order to simplify the definition of boundary conditions, it is common to define a modified pressure as

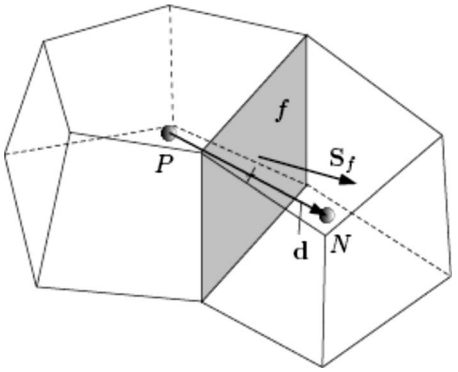

FIG. 5. Discretization of the solution domain.

$$p_d = p - \rho \mathbf{g} \cdot \mathbf{x}, \tag{19}$$

where **x** is the position vector. It can be easily shown that the gradient of modified pressure p_d consists of the static pressure gradient, the body force due to gravity and an additional contribution originating from the density gradient. In order to satisfy the momentum equation, the pressure gradient is expressed using Eq. (19) whereas the momentum equation is rearranged to read [30]

$$\frac{\partial(\rho \mathbf{U})}{\partial t} + \nabla \cdot (\rho \mathbf{U}\mathbf{U}) - \nabla \cdot (\mu \nabla \mathbf{U}) - (\nabla \mathbf{U}) \cdot \nabla \mu = -\nabla p_d - \mathbf{g} \cdot \mathbf{x} \nabla \rho + \sigma \kappa \nabla \gamma. \tag{20}$$

Body forces due to pressure gradient and gravity are implicitly accounted for by the first two terms on the right-hand side of the Eq. (20). Summing up, the present mathematical model is given by the continuity equation, Eq. (7), phase fraction equation, Eq. (15), and momentum equation, Eq. (20).

The model is closed by supplying an appropriate expression for the compression velocity $\mathbf{U}_r$. In order to ensure that this velocity does not bias the solution in any way, it must act only in the perpendicular direction to the interface. Furthermore, by inspection of Eq. (15) it is evident that only the values of $\mathbf{U}_r$ on the grid cell faces will be used, being in accordance with the discretization of the convective term. The model for $\mathbf{U}_r$ is described in detail in Sec. IV B 2.

B. Computational method

1. Numerical setup and discretization

All computations are performed using the code OpenFOAM [36], an open source computational fluid dynamics (CFD) toolbox, utilizing a cell-center-based finite volume method on a fixed unstructured numerical grid and employing the solution procedure based on the pressure implicit with splitting of operators (PISO) algorithm for coupling between pressure and velocity in transient flows [37]. The solution domain is subdivided into a number of cells with computational points placed at cell centroids. Each two cells share exactly one cell face, on which a face surface normal vector is defined, as shown in Fig. 5.

The flow domain considered in the present simulations has the form of an axisymmetric slice with only one cell in the azimuthal direction, Fig. 6. Hereby, the symmetry in azimuthal direction is presumed in accordance with the experimental observations. The dimensions of the solution domain are 45 mm × 45 mm in the vertical plane, yielding the corresponding normalized lengths of $15D \times 15D$ for distilled water, $21D \times 21D$ for isopropanol and $17D \times 17D$ for glycerin-water mixture. The grid is adaptively refined in the region of the crater development.

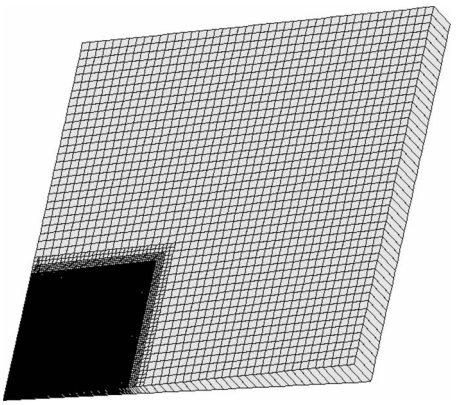

FIG. 6. Computational grid.

It could be observed in experiments, as well as in the previous calculations on coarser grids, that the liquid film was not significantly affected at radial distances greater than approximately one third of the radial length of the solution domain, since the process of drop impact occurs very fast. Therefore the grid was appropriately refined only in this region of the solution domain, where the process of drop impact takes place.

The equations are discretized following the finite volume technique. The transient and source terms are discretized using the midpoint rule and integrated over cell volumes. Time derivative terms are discretized using an implicit Euler scheme. The terms comprising spatial derivatives, as diffusion and convective terms, are converted into integrals over surfaces bounding each cell using Gauss' theorem. The integration is performed by summing values at cell faces, obtained by interpolation. For the evaluation of gradients a linear face interpolation is used.

In order to account for the nonorthogonal contribution, a correction term is included in the calculation of gradients at cell faces, evaluated by interpolating cell center gradients. In the discretization of the convective terms, boundedness of the solution is assured by using a face interpolation based on normalized variable diagram (NVD). A high resolution differencing scheme was used [38], with a limiter evaluated based on the ratio between volume flux gradients calculated at adjacent cell faces and cell centers. The interpolated face value ϕ_f of a variable ϕ, which is calculated at computational points P and N in Fig. 5, is obtained from the expression

$$\phi_f = \lambda(\phi_P - \phi_N) + \phi_N, \tag{21}$$

where λ is a weighting factor calculated using flux limiter (blending factor) ψ from the limited scheme [38] and weighting factor $f_{\mathbf{d}}$ of a linear interpolation scheme,

$$\lambda = \psi f_{\mathbf{d}} + (1 - \psi)\Pi(\mathbf{U}_f \cdot \mathbf{S}_f). \tag{22}$$

where $f_{\mathbf{d}} = \overline{fN}/\overline{PN}$, and the operator $\Pi(\mathbf{U}_f \cdot \mathbf{S}_f)$ is a switch, which accounts for the flow direction defined as

$$\Pi(\mathbf{U}_f \cdot \mathbf{S}_f) = \begin{cases} 1, & \text{for } \mathbf{U}_f \cdot \mathbf{S}_f > 0 \text{ (the flow is from } P \text{ to } N) \\ 0, & \text{for } \mathbf{U}_f \cdot \mathbf{S}_f < 0 \text{ (the flow is from } N \text{ to } P). \end{cases} \tag{23}$$

2. Discretization of the "compression term"

For the discretization of the compression term in Eq. (15) the relative velocity at cell faces, formulated based on the maximum velocity magnitude at the interface region and its direction, is determined from the gradient of phase fraction as follows:

$$U_{r,f} = n_f \min\left[C_\gamma \frac{|\phi|}{|\mathbf{S}_f|}, \max\left(\frac{|\phi|}{|\mathbf{S}_f|} \right) \right], \tag{24}$$

where ϕ is face volume flux, and n_f is face unit normal flux, calculated at cell faces in the interface region using the phase fraction gradient at cell faces,

$$n_f = \frac{(\nabla \gamma)_f}{|(\nabla \gamma)_f + \delta_n|} \cdot \mathbf{S}_f. \tag{25}$$

In the normalization of the phase fraction gradient in Eq. (25) and Eq. (17), a stabilization factor δ_n is used, which accounts for nonuniformity of the grid,

$$\delta_n = \frac{\varepsilon}{\left(\frac{\sum_N V_i}{N} \right)^{1/3}}, \tag{26}$$

where N is the number of computational cells and ε is a small parameter, set to 10^{-8} here.

The model is relatively simple and robust, relying basically on the definition of the velocity in Eq. (14). If there is a small bulk motion of the gaseous phase in the vicinity of the free surface, the relative velocity will be close to the velocity of the liquid phase. If the velocities of both phases are of the same order of magnitude, the intensity of the free surface compression is controlled by the constant C_γ, which yields no contribution if set to zero, a conservative compression if the value is one (as used in the present study), and enhanced compression for values greater than one [39]. It should be noted that the face volume flux in Eq. (24) is not evaluated using the face interpolation of the velocity, but is determined as a conservative volume flux resulting from the pressure-velocity coupling algorithm.

3. Adaptive time step control

In order to ensure stability of the solution procedure, the calculations are performed using a self-adapting time step which is adjusted at the beginning of the time iteration loop based on the Courant number defined as

$$\mathrm{Co} = \frac{|\mathbf{U}_f \cdot \mathbf{S}_f|}{\mathbf{d} \cdot \mathbf{S}_f} \Delta t, \tag{27}$$

where $\mathbf{d}$ is a vector between calculation points of control volumes sharing the face, i.e., $\mathbf{d} = \overline{PN}$ and Δt is time step. Using values for $\mathbf{U}_f$ and Δt from previous time step, a maximum local Courant number Co^o is calculated and the new time step is evaluated from the expression

$$\Delta t^n = \min\left\{ \frac{\mathrm{Co}_{max}}{\mathrm{Co}^o} \Delta t^o, \left(1 + \lambda_1 \frac{\mathrm{Co}_{max}}{\mathrm{Co}^o} \right) \Delta t^o, \lambda_2 \Delta t^o, \Delta t_{max} \right\}, \tag{28}$$

where Δt_{max} and Co_{max} are prescribed limit values for the time step and Courant number, respectively.

According to this prescription the new time step will decrease if Co^o overshoots Co_{max} and increase otherwise. To avoid time step oscillations that may lead to instability, the increase of the time step is damped using factors λ_1 and λ_2, according to the conditions in Eq. (28).

It was found by experience in test calculations that the limit value for the Courant number should not exceed $\mathrm{Co}_{max} \approx 0.2$, which is the value also used in this study, and values for damping factors are $\lambda_1 = 0.1$ and $\lambda_2 = 1.2$. Using the above prescription, the time step is adjusted smoothly, keeping the maximum local Courant number nearly equal to the prescribed limit value.

However, at the startup of the simulation, usually some very small initial time step Δt_{init} is used, which could lead to a very small maximum local value of the Courant number and a new time step that would be too large for the start, and vice versa. Therefore, at the beginning of the calculation an intermediate value for the initial time step is calculated as

$$\Delta t^*_{init} = \min\left(\frac{\mathrm{Co}_{max} \Delta t_{init}}{\mathrm{Co}^o}; \Delta t_{max} \right). \tag{29}$$

This intermediate value is than used as Δt^o in Eq. (28) providing the value of Co^o for the first time step to be close to the prescribed limit value Co_{max}. The size of the time steps was varying during calculations between values on the order of 10^{-7} s to 10^{-5} s.

4. Temporal subcycling

It is common in VOF-based methods that the convergence and stability of the solution procedure are very sensitive with respect to the equation for phase fraction. Bounded discretization schemes for divergence terms and time step control are both used to overcome these difficulties and, although it is generally recommended to keep the maximum local Courant number much below unity, it is beneficial to solve the phase fraction equation in several subcycles within a single time step. The time step to be used in a single time subcycle is set by dividing the global time step by the preset number of subcycles,

$$\Delta t_{sc} = \frac{\Delta t}{n_{sc}}. \tag{30}$$

After the phase fraction γ in each subcycle is updated, a corresponding mass flux $F_{sc,i}$ through cell faces is calculated.

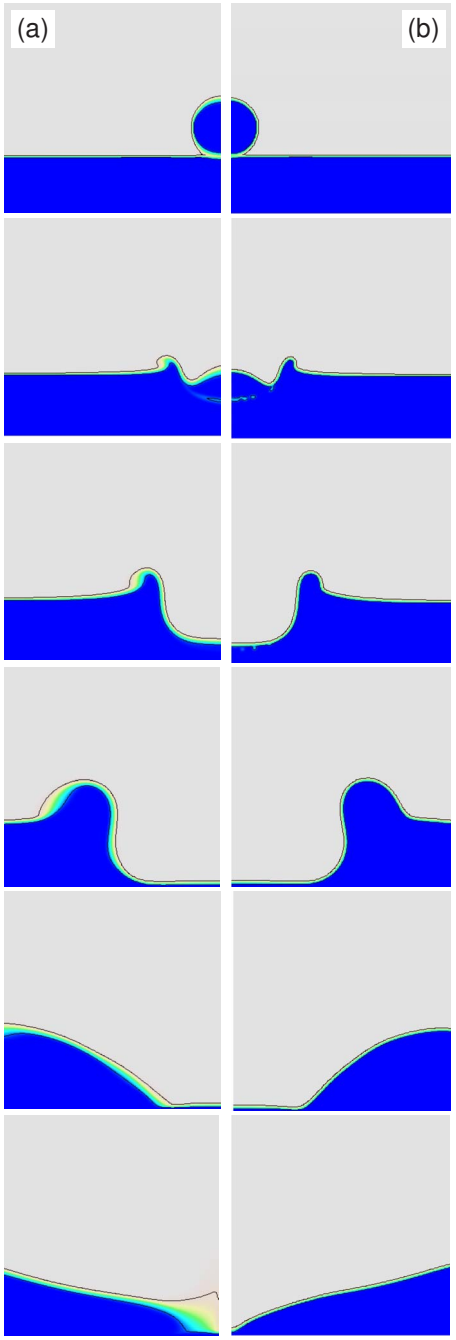

FIG. 7. (Color online) Time evolution of the crater shape for the impact of a glycerin-water mixture drop, $\bar{H}=1$, We=329, Re=428, $K=1182$: results obtained by (a) the conventional VOF model and (b) advanced model. The time sequences from top to bottom correspond to $tU/D=0,0.99,2.47,9.89,19.76,28.67$.

The total mass flux F corresponding to the global time step, which is needed in the momentum equation, is then obtained from

$$F=\rho\mathbf{U}_f\cdot\mathbf{S}_f=\sum_{i=1}^{n_{sc}}\frac{\Delta t_{sc}}{\Delta t}F_{sc,i}. \tag{31}$$

In addition to providing a more accurate solution of the phase fraction equation, this algorithm also enables the global time step size to be greater for the solution of other transport equations, thereby considerably speeding up the solution procedure.

5. Initial and boundary conditions

At the initial time (before the impact occurs), the distribution of volume fraction is prescribed throughout the domain, defining the position and the shape of the interface (consisting of the drop surface and the film surface) at the beginning of the calculation. In order to minimize the initialization errors, the pressure within the drop is set equal to capillary pressure corresponding to the drop diameter. The shape of the drop in experiments just before the impact deviated negligibly from that of a sphere. Therefore, the drop in simulations is placed at a small initial distance from the film surface corresponding to a nondimensional time of $tU/D=0.2$, thus allowing several time steps to be computed and the flow to develop before the first contact of the drop with the surface. Since the distance is very small the velocity change due to the gravity and drag is negligibly small. The initial drop velocity is thus set equal to the drop impact velocity from experiments.

In addition to the axial symmetry, the no-slip condition is prescribed at the bottom and on the right side boundary of Fig. 6. The top boundary is open with prescribed total pressure consisting of static and dynamic pressure, thus allowing the static pressure to be adjusted according to the calculated velocity field. At the walls a zero gradient is set for the modified pressure, which is in accordance to the definition in Eq. (19).

Since the contact region of the crater with the bottom of the dish could not clearly be observed in the experiments, it was not possible to discern whether the bottom surface remained wetted or became completely or partially dry. Therefore, wall adhesion was not taken into account and correspondingly a zero-gradient condition for the volume fraction equation is set.

V. RESULTS AND DISCUSSION

A. Validation of the advanced algorithm

For the purpose of the comparison between the classical VOF approach and the advanced model used presently, the simulations of a selected drop impact case using both models are performed. The case in question corresponds to the glycerin-water mixture and impact parameters $\bar{H}=1$, We =329, and Re=428. The results obtained are contrasted in Fig. 7. The interface region is situated between black lines indicating the region of the free surface, corresponding to the values of phase fraction equal to 0.1 and 0.9. All details describing the case considered with respect to the computational mesh, initial and boundary conditions, dimensionless numbers, and physical properties are equal in both simulations. It can be clearly seen that the interface region captured using the advanced model exhibits much higher resolution during all stages after impact. This can be observed even at the time corresponding to the first contact between drop and the film, where the interface already appears more smeared

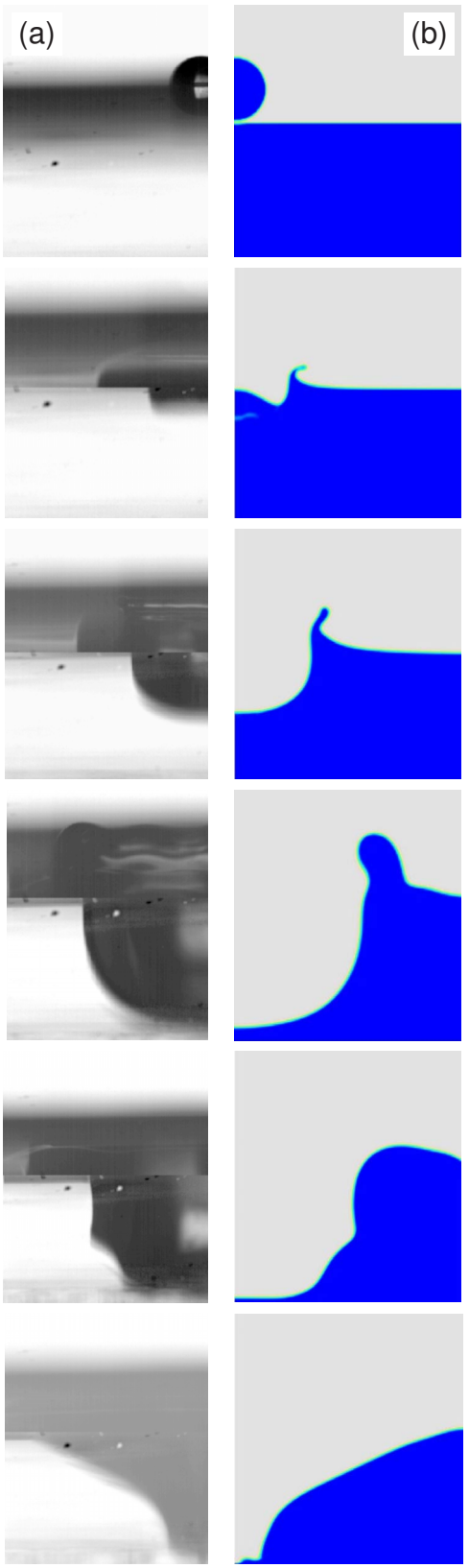

FIG. 8. (Color online) Time evolution of the crater shape for the impact of an isopropanol drop, $\bar{H}=2$, We=392, Re=1730, $K=2364$: (a) experiment and (b) simulations. The time sequences from top to bottom correspond to $tU/D=0,1.08,2.71,10.84,21.68,31.44$.

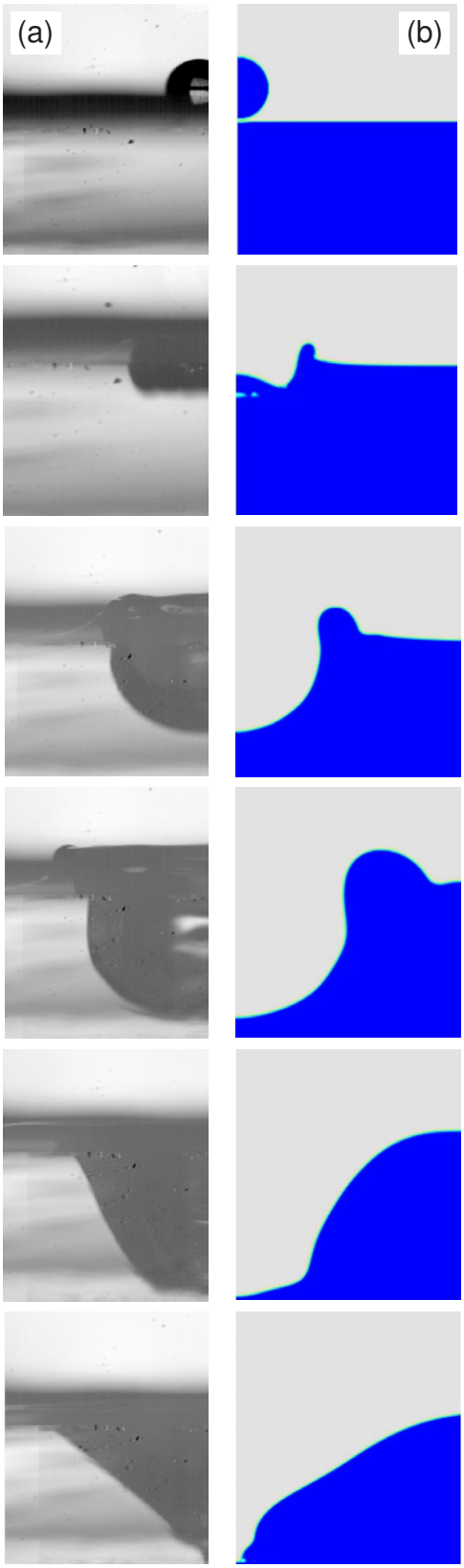

FIG. 9. (Color online) Time evolution of the crater shape for the impact of a distilled water drop, $\bar{H}=2$, We=215, Re=6750, $K=2533$: (a) experiment and (b) simulations. The time sequences from top to bottom correspond to $tU/D=0,1.21,4.03,8.06,16.13,20.97$.

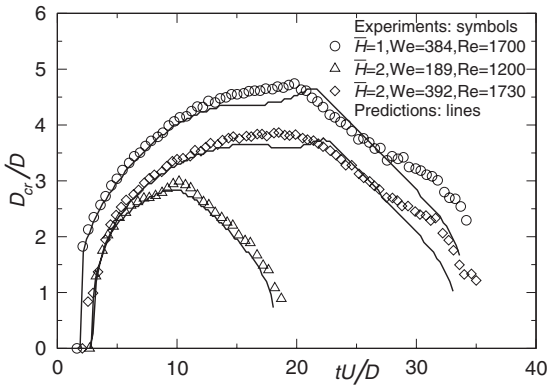

FIG. 10. Experimentally and computationally obtained dimensionless crater diameter for the impact of an isopropanol drop.

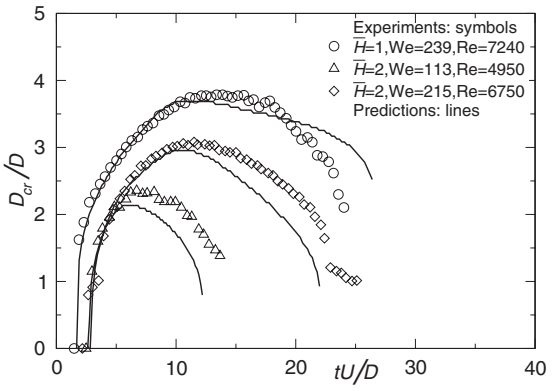

FIG. 12. Experimentally and computationally obtained dimensionless crater diameter for the impact of a distilled water drop.

in the case of the conventional VOF method. The solution at later stages becomes nonphysical, as can be seen for instance at $tU/D=28.67$. On the other hand the application of the advanced model leads to a physically plausible solution and a much sharply resolved free surface. Accordingly, all computational results displayed in the reminder of the manuscript and discussed along the experimental database have been obtained using the advanced algorithm.

B. Penetration and expansion of the crater

First comparison between experiments and simulations relates to the time evolution of the crater shape. Figure 8 and Fig. 9 show the crater shape at different time instants for the flow configuration corresponding to $\bar{H}=2$ for isopropanol and distilled water, respectively. Immediately upon impact, a small circumferential free liquid jet is ejected upward. The geometry of this free jet (its height, shape, and width) depends on the drop impact velocity, liquid properties, and liquid film thickness. Inside the liquid film the drop impact leads to the formation of a cavity (crater), which penetrates into the film and simultaneously expands radially. During the spreading period inertial forces are dominant over viscous and capillary forces since the Weber number is much higher than unity.

After reaching the maximum diameter, the crater begins a receding motion driven by capillary forces. It can be seen that the crater shape changes from a spherical form in the advancing motion to a conical one during the receding phase. The results of simulations indicate also that during the first stages of impact the cavity has a concave surface in its upper part. Afterwards, the crater is fully formed until its bottom becomes convex. This could not be observed in experiments due to capillary rise of the liquid film meniscus at the side walls of the dish where it was placed, and consequently, for the purpose of comparison, the measured crater depth is related to the lowest point at the surface of the crater obtained in the simulations. The present axisymmetric simulations are not capable of describing precisely the three-dimensional nature of the flow in the uprising jet leading to the rim instability and in some cases to splash. For capturing such effects a full three-dimensional computational model would be required, accompanied by additional considerations of physical perturbations leading to instability. Moreover, the exact shape of this jet cannot be easily compared with the experiments since the camera is focused on the crater, which is the main object of the present study. Nevertheless, the influence of the three-dimensional effects on the dynamics of the crater propagation is regarded to be small in the considered range of the drop impact parameters. This assumption is further confirmed by correctly capturing the generation and propagation of the capillary wave in the falling jet.

For the purpose of a quantitative analysis, crater depth and diameter are made dimensionless through division by

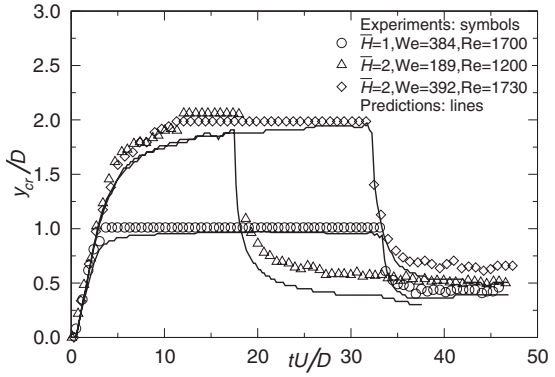

FIG. 11. Experimentally and computationally obtained dimensionless crater depth for the impact of an isopropanol drop.

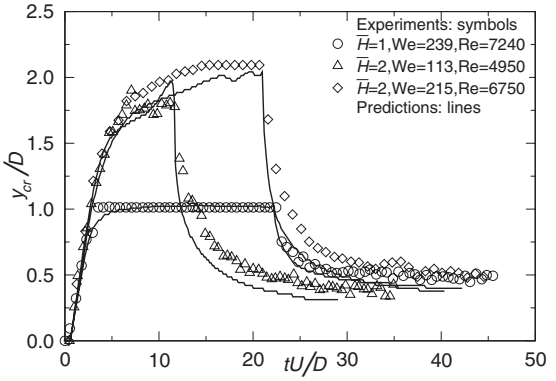

FIG. 13. Experimentally and computationally obtained dimensionless crater depth for the impact of a distilled water drop.

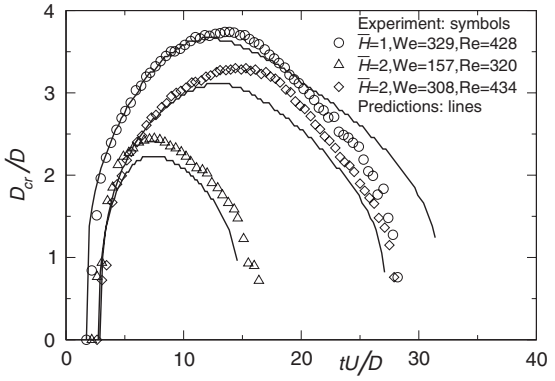

FIG. 14. Experimentally and computationally obtained dimensionless crater diameter for the impact of a glycerin-water mixture drop.

drop diameter, and the measured values are compared to predicted ones. In the experiments the depth is measured at the lowest point of the crater observed in photographs, and the diameter is determined at a half film thickness, i.e., for $y/H=0.5$, where y is the vertical distance measured from the free surface of the film. In simulations, depth and diameter are determined using computational cells where volume fraction becomes $\gamma \geqslant 0.5$.

Plots of dimensionless crater diameter and depth against dimensionless time are shown in Fig. 10 and Fig. 11 for isopropanol, in Fig. 12 and Fig. 13 for distilled water, and in Fig. 14 and Fig. 15 for the glycerin-water mixture, respectively. The agreement between the theoretical predictions and the experimental data is rather good.

C. Residual thickness of the film between the crater and the bottom

When the crater approaches the bottom the penetration velocity decreases due to the wall effects. When the inertia of the liquid flow is strong enough, the thickness of the film below the cavity follows the remote asymptotic solution [11] and decreases as the inverse of the time squared.

At some time instant the film thickness becomes comparable with the thickness of the viscous boundary layer. The flow in the film is damped by viscosity. The remaining thin film thickness is much smaller than the initial thickness of the liquid layer. This phase corresponds to the "plateau" region in graphs shown in Figs. 11, 13, and 15.

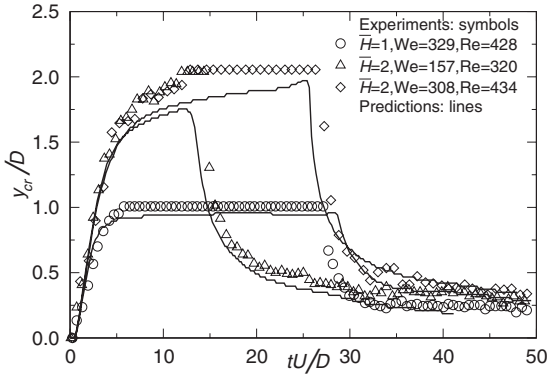

FIG. 15. Experimentally and computationally obtained dimensionless crater depth for the impact of a glycerin-water mixture drop.

TABLE II. Residual film thickness predicted using the numerical simulations at various impact parameters.

Liquid	We	Re	K	$\bar{H}$	$\bar{h}_{res}$
Isopropanol	384	1700	2238	1	0.01631
Isopropanol	189	1200	1101	2	0.05650
Isopropanol	392	1730	2364	2	0.04425
Distilled water	239	7240	2815	1	0.00449
Distilled water	113	4950	1331	2	0.02802
Distilled water	215	6750	2533	2	0.01796
Glycerin water mixture	329	428	1182	1	0.01534
Glycerin water mixture	157	320	564	2	0.09206
Glycerin water mixture	308	434	1106	2	0.08193

The value of the residual film thickness is rather important for the modeling of heat transfer associated with drop or spray impact and prediction of the film breakup. Unfortunately, since the residual film thickness is much smaller than the initial drop diameter and the initial film thickness, its experimental evaluation is not an easy task. In the present study this value is determined from the numerical simulations. The predicted values of the residual film thickness $\bar{h}_{res}$ $(=h_{res}/D)$ are given in Table II for various impact parameters.

The dimensionless time $\bar{t}_b$ at which the crater almost reaches the bottom lies within the interval $12<\bar{t}_b<14$ for $\bar{H}=2$ and $3<\bar{t}_b<5$ for $\bar{H}=1$. The thickness of the boundary layer at this time instant is approximately $\bar{h}_{bl}\sim\sqrt{\bar{t}_b/\mathrm{Re}}$.

When the crater approaches the bottom, the film thickness follows the remote asymptotic solution [11]. At larger times after impact it can be written in the simplified form

$$\bar{h}_{cr}=\bar{H}-\bar{y}_{cr}\sim\bar{t}^{-2}, \tag{32}$$

$$\bar{U}_{cr}=\frac{d\bar{h}_{\mathrm{cr}}}{dt}\sim\bar{t}^{-3}. \tag{33}$$

Therefore, the time instant at which the boundary layer reaches the free surface of the cavity is $\bar{t}_{bl}\sim\mathrm{Re}^{1/5}$ and the crater velocity at this instant is $\bar{U}_{cr}\sim\mathrm{Re}^{-3/5}$. The film thickness $\bar{h}_{bl}$ corresponding to the time instant $\bar{t}_{bl}$ can be easily estimated from Eq. (32) as $\bar{h}_{bl}\sim\mathrm{Re}^{-2/5}$.

The residual film thickness is smaller than $\bar{h}_{bl}$ since the inertia of the fluid at the time instant $\bar{t}=\bar{t}_{bl}$ is still significant. The value of the residual film thickness is estimated assuming the creeping flow in the film [40] in the following form:

$$\bar{h}_{res}=\frac{\bar{h}_{bl}^{9/14}}{\left(\frac{1}{\bar{h}_{bl}}+\frac{14\,\mathrm{Re}\,\bar{U}_{cr}}{15}\right)^{5/14}}. \tag{34}$$

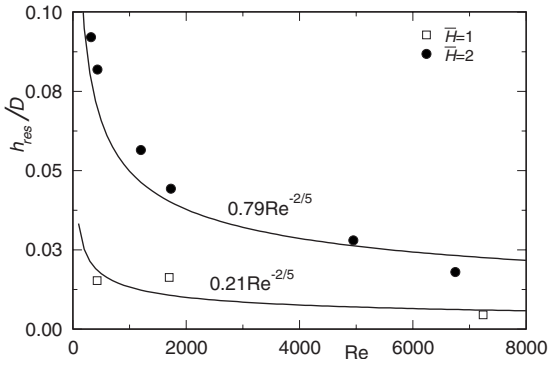

FIG. 16. Computationally obtained residual film thickness under the cavity as a function of the impact Reynolds number compared to the present measurements.

Our scaling analysis leads to the following relation between the residual film thickness and the Reynolds number,

$$\bar{h}_{res} = A\,\mathrm{Re}^{-2/5}. \tag{35}$$

The coefficient A depends on the dimensionless initial film thickness, Weber and Froude numbers. However, the dependency on We and Fr is weak if they are much larger than the unity. Figure 16 displays the comparison of the numerically predicted residual film thickness with the present experimental data in terms of the impact Reynolds number. The scaling relation (35) describes well the tendency of the obtained results.

After some period of time the capillary forces become significant and the crater starts to contract, leading to the emergence of a central jet. The crater contraction starts earlier at impact parameters corresponding to smaller Weber numbers (for which the influence of the surface tension is more significant).

The evolution of the diameter of the crater first follows the well-known square-root dependence law obtained from the remote asymptotic solution [11]. At longer times its propagation is governed by surface tension and gravity [41]. The maximum crater diameter and the corresponding duration of the crater expansion and merging are mainly determined by the impact Weber number.

D. Pressure and velocity fields

Computationally obtained pressure and velocity fields for impact of isopropanol drop at $\bar{H}=2$, We=392, and Re =1730 are shown in Fig. 17 and Fig. 18, respectively, at several stages of the impact including the time instant corresponding to the very beginning of the drop impingement onto the film surface. For the sake of clarity, the velocity vectors are plotted using randomly spaced tracers. The experimental data for these parameters cannot be easily collected. On the other hand the knowledge about the pressure magnitudes in the flow is rather important for the modeling of the substrate erosion, splash, spray cleaning, drop impact onto a porous or elastic target, etc. A detailed description of the velocity field in the film initiated by drop impact is necessary for the reliable modeling of hydrodynamics of spray coating and spray cooling.

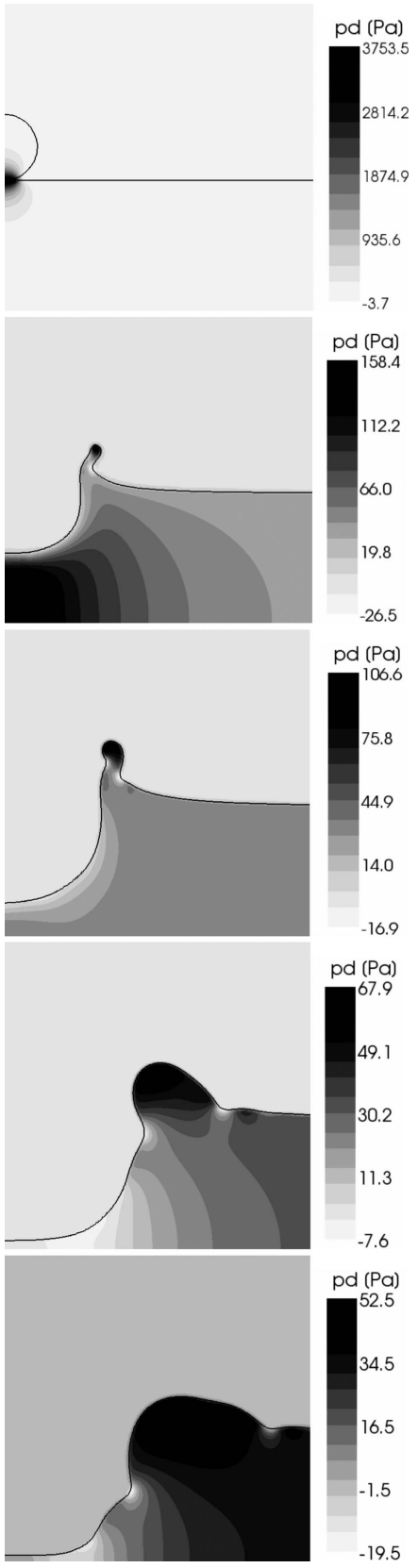

FIG. 17. Predicted isocontours of the pressure field for the impact of an isopropanol drop: $\bar{H}=2$, We=392, Re=1730, $K=2364$. The time instants from top to bottom correspond to tU/D $=0, 2.71, 5.42, 16.26, 21.68$.

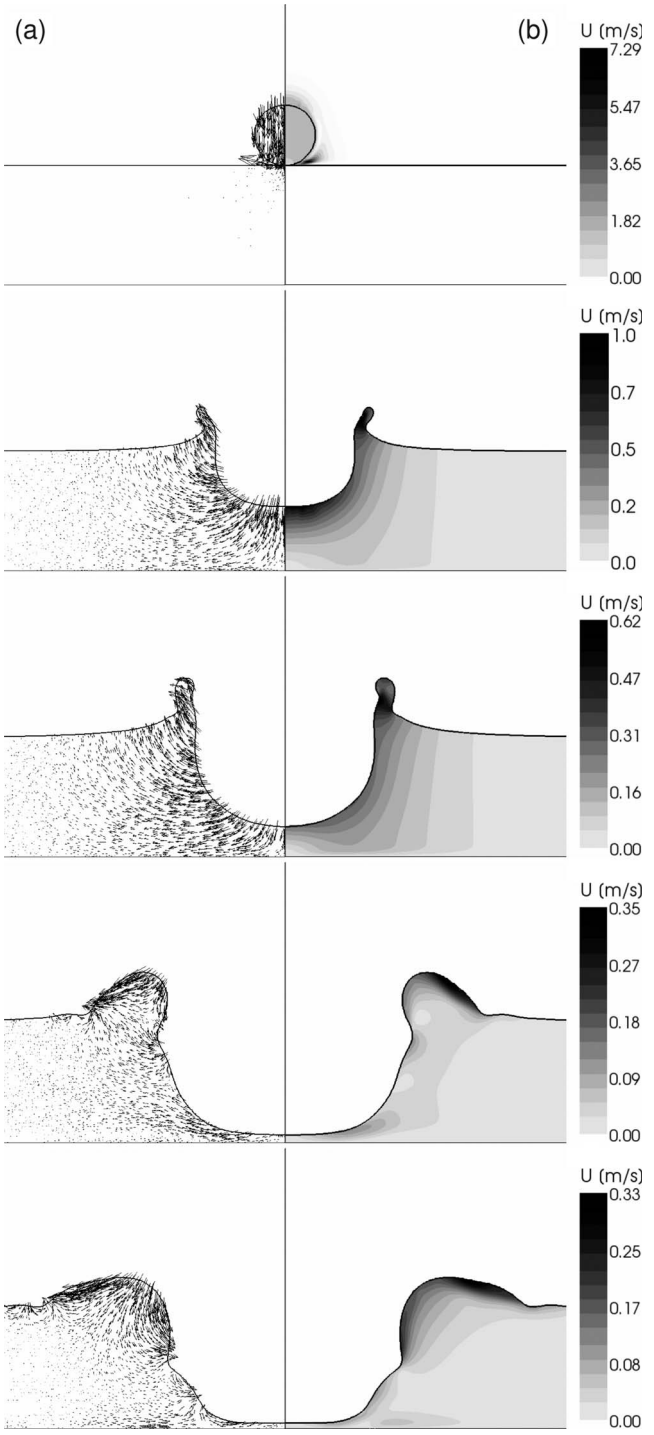

FIG. 18. Predicted velocity vectors (a) and isocontours of velocity magnitude (b) for the impact of an isopropanol drop: $\bar{H}=2$, We=392, Re=1730, $K=2364$. The time instants from top to bottom correspond to $tU/D=0,2.71,5.42,16.26,21.68$.

The pressure distribution at various instants of time is shown in Fig. 17. It can be seen that at the moment when the drop touches the liquid film, a high pressure is formed in the region of contact. As a consequence of this, the liquid is ejected in a radially upward direction. As the drop penetrates into the film, the liquid sheet straightens, driven by the local velocity field and a small deviation of the inner part of the sheet surface is observed. A relatively high pressure region can be identified at the edge of the uprising sheet. This region with the relatively high curvature corresponds to the formation of a rim [24]. The velocity of the rim differs from the velocity of the sheet since its dynamics is determined mainly by the capillary forces. The pressure in the rim is not uniform despite the fact that the curvature of the rim surface does not change significantly. The pressure gradient inside the rim is caused by its acceleration in the downward direction. It is interesting to note that the pressure in the rim remains almost constant even at the later stages of the sheet motion when the radius of the rim cross section is relatively high.

The velocity field confined to the region occupied by the liquid at various time instants is shown in Fig. 18. At the moment when the drop hits the liquid film the air velocities near the free surfaces are also shown, indicating a high speed flow of the air escaping from the space between the falling drop and the liquid film. The vector plots and velocity magnitudes at the initial stages upon the impact show a radially outward oriented velocity distributions, with respect to the origin coinciding with the point of impact, thereby resembling closely the theoretically assumed potential flow in the liquid near the cavity surface. This also confirms the assumption of the velocity of the effective fluid in simulations as a weighted average of liquid and gas velocities, and the assumption that the evolution of the free surface is mainly caused by the velocity of the liquid in the region near the free surface. Furthermore, the reduction of the velocity magnitude in time can be observed as the cavity is decelerating. At later stages the velocity distribution becomes more complex, including some vortexlike motions, and cannot be approximated using a simple velocity potential.

E. Initiation of the capillary wave

One of the most spectacular phenomena related to drop impact onto a liquid film is the generation of a rather sharp capillary wave on the surface of the crater. It is interesting that once the wave is created, its outer corner is rather sharp, indicating a strong local pressure drop. The wave propagates along the cavity surface downwards, merging at the bottom of the crater and finally leads to the creation of a central jet [42]. Similar waves have been observed in many experiments on drop impact onto a liquid layer or liquid pool [7,9,10]. The mechanism of the formation of these capillary axisymmetric waves and their propagation is not immediately clear.

Such a capillary wave is observed at the surface of the crater in Fig. 8. It is created inside the uprising sheet and travels downwards along the crater surface. This behavior is clearly resolved in the simulations. The capillary wave is observed here only when isopropanol is used, whereas it could not clearly be seen in impacts of distilled water and glycerin-water mixture. This is explained by the much lower surface tension of isopropanol.

In the case shown in Fig. 17, the moment at which the capillary wave can first clearly be seen corresponds to a dimensionless time of approximately 5.42. At this instant the

rim formed at the edge of the uprising sheet merges with the liquid film. In this instant the pressure inside the rim is elevated. It corresponds to the curvature of the rim cross section and its acceleration. The flow in the rim is directed downwards. The capillary wave separates the high pressure region above and the relatively lower pressure region below the wave. The high pressure region above leads to the deformation of the shape of the cavity behind the wave. Moreover, the pressure difference ahead and behind the wave leads to the liquid acceleration and enhances the wave propagation.

VI. CONCLUSIONS

In this paper the dynamics of the crater formed upon the impact of a single drop onto a liquid film was investigated using experimental measurements and numerical simulations. The dynamics of drop impact on liquid surfaces is analyzed, focusing on the evolution of the crater formed beneath the surface upon the impact.

A theoretical model is developed for the penetration of the crater at the initial stage. The shape of the crater is approximated by a spherical cavity and the velocity field past the propagating crater is approximated by the potential flow. The equations of motion of the crater tip are obtained from the pressure balance at this point. The asymptotic solution is obtained by neglecting capillary, viscous, and gravity effects. The agreement with the experimental data is very good.

An advanced model for the free surface capturing within the numerical framework is used, based on a two-fluid formulation of the conventional volume-of-fluid model and very good agreement between experiments and simulations is obtained. It is confirmed that increasing the impact velocity at a constant film thickness has little to no effect on the crater evolution in depth and on the time to reach maximum depth. For lower impact velocities, the moment at which the crater starts to retract is sooner and the collapse is faster. For larger impact velocities, the value of the maximum diameter is higher and it is reached at a later time instant. An increase in the film thickness leads to a longer time needed for the crater to reach the bottom. For the same film thickness, the crater reaches the bottom at approximately the same time. The surface tension has a clear influence on the receding motion of the crater and the decrease in diameter, as for higher values of surface tension the decrease starts earlier and is somewhat steeper.

The numerical simulations demonstrate not only high level of the predictive capabilities of the advanced model resolving the free surface, they also help to better understand the mechanisms of crater evolution. In particular the formation and propagation of the capillary wave along the cavity surface could be explained using the results of the numerical predictions of the pressure field in the liquid. Moreover, the results of numerical predictions eventually help to understand the flow in the liquid during the impact, since no detailed experimental data for the distributions of pressure and velocity is available.

Scaling relations for the residual film thickness have been proposed based on the description of the film evolution and development of the viscous boundary layer. This data can be valuable in the modeling of spray cooling.

ACKNOWLEDGMENTS

The authors would like to acknowledge DAAD (Deutscher Akademischer Austauschdienst) for sponsoring E. Berberović. The authors would also like to acknowledge the German Scientific Foundation (DFG) for financial support in the framework of the Collaborative Research Center 568 (Grant No. TP A1) and in the framework of research Grant No. Tr 194/34.

[1] M. Rein, Fluid Dyn. Res. **12**, 61 (1993).
[2] A. L. Yarin, Annu. Rev. Fluid Mech. **38**, 159 (2006).
[3] J. Shin and T. A. McMahon, Phys. Fluids A **2**, 1312 (1990).
[4] A. I. Fedorchenko and A. B. Wang, Phys. Fluids **16**, 1349 (2004).
[5] W. C. Macklin and P. V. Hobbs, Science **166**, 107 (1969).
[6] H. N. Oguz and A. Prosperetti, J. Fluid Mech. **228**, 417 (1991).
[7] D. Morton, M. Rudman, and L. J. Leng, Phys. Fluids **12**, 747 (2000).
[8] Z. Mohamed-Kassim and E. K. Longmire, Phys. Fluids **16**, 2170 (2004).
[9] Q. Deng, A. V. Anilkumar, and T. G. Wang, J. Fluid Mech. **578**, 119 (2007).
[10] L. J. Leng, J. Fluid Mech. **427**, 73 (2001).
[11] A. L. Yarin and D. A. Weiss, J. Fluid Mech. **283**, 141 (1995).
[12] D. A. Weiss and A. L. Yarin, J. Fluid Mech. **385**, 229 (1999).
[13] M. Bussmann, S. Chandra, and J. Mostaghimi, Phys. Fluids **12**, 3121 (2000).
[14] N. Nikolopoulos, A. Theodorakakos, and G. Bergeles, J. Comput. Phys. **225**, 322 (2007).
[15] C. Josserand and S. Zaleski, Phys. Fluids **15**, 1650 (2003).
[16] C. Mundo, M. Sommerfeld, and C. Tropea, Atomization Sprays **8**, 625 (1998).
[17] O. G. Engel, J. Appl. Phys. **38**, 3935 (1967).
[18] H. C. Pumphrey and P. A. Elmore, J. Fluid Mech. **220**, 539 (1990).
[19] A. Prosperetti and H. N. Oguz, Annu. Rev. Fluid Mech. **25**, 577 (1993).
[20] G. Birkhoff, D. P. MacDougall, E. M. Pugh, and G. Taylor, J. Appl. Phys. **19**, 563 (1948).
[21] A. L. Yarin, M. B. Rubin, and I. V. Roisman, Int. J. Impact Eng. **16**, 801 (1995).
[22] F. Batchelor, *An Introduction to Fluid Mechanics* (Cambridge Universty Press, Cambridge, 1970).
[23] P. A. Elmore, G. L. Chahine, and H. N. Oguz, Exp. Fluids **31**, 664 (2001).
[24] G. Taylor, Proc. R. Soc. London, Ser. A **253**, 296 (1959).
[25] C. W. Hirt and B. D. Nichols, J. Comput. Phys. **39**, 201 (1981).
[26] S. Muzaferija and M. Perić, in *Nonlinear Water Wave Interaction*, edited by M. M. O. Mahrenholtz (WIT Press, Southamp-

tion, UK, 1999), pp. 59–100.
[27] R. Scardovelli and S. Zaleski, Annu. Rev. Fluid Mech. **31**, 567 (1999).
[28] S. Afkhami and M. Bussmann, Int. J. Numer. Methods Fluids **57**, 453 (2008).
[29] S. J. Cummins, M. M. Francois, and D. B. Kothe, Comput. Struct. **83**, 425 (2005).
[30] H. Rusche, Ph.D. thesis, Imperial College of Science, Technology and Medicine, London, 2002.
[31] OpenCFD Ltd., 2007, http://www.opencfd.co.uk/
[32] G. Černe, S. Petelin, and I. Tiselj, J. Comput. Phys. **171**, 776 (2001).
[33] OpenCFD, Technical Report No. TR/HGW/02, 2005 (unpublished).
[34] O. Ubbink and R. I. Issa, J. Comput. Phys. **153**, 26 (1999).
[35] J. U. Brackbill, D. B. Kothe, and C. Zemach, J. Comput. Phys. **100**, 335 (1992).
[36] H. G. Weller, G. Tabor, H. Jasak, and C. Fureby, Comput. Phys. **12**, 620 (1998).
[37] R. I. Issa, J. Comput. Phys. **62**, 40 (1986).
[38] H. Jasak, H. G. Weller, and A. D. Gosman, Int. J. Numer. Methods Fluids **31**, 431 (1999).
[39] OpenCFD Ltd, OpenFOAM, The Open Source CFD Toolbox, User Guide, OpenCFD Ltd., 2008, http://www.opencfd.co.uk/openfoam/
[40] S. Bakshi, I. V. Roisman, and C. Tropea, Phys. Fluids **19**, 032102 (2007).
[41] I. V. Roisman, N. P. vanHinsberg, and C. Tropea, Phys. Rev. E **77**, 046305 (2008).
[42] F. H. Zhang and S. T. Thoroddsen, Phys. Fluids **20**, 022104 (2008).